OES | Opto-Electronic Science

Narrow beam and low-sidelobe electro-optic beam steering on thin-film lithium niobate optical phased array

Yang Li, Shiyao Deng, Xiao Ma, Ziliang Fang, Shufeng Li, Weikang Xu, Fangheng Fu, Xu Ouyang, Yuming Wei, Tiefeng Yang, Heyuan Guan* and Huihui Lu*

https://doi.org/10.29026/oes.2026.260002

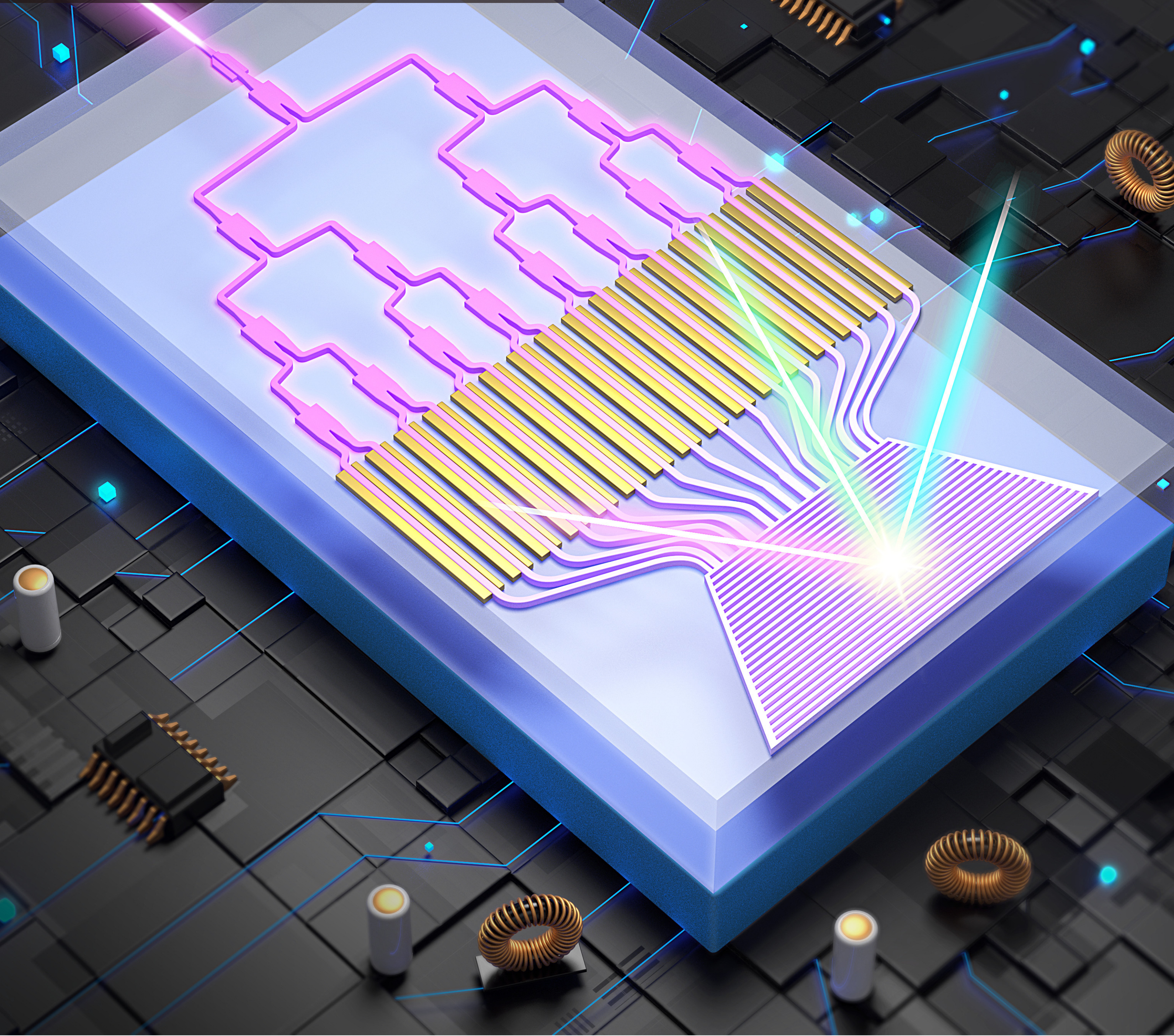

Opto-Electronic Science

CN 51-1800/O4 ISSN (Print) 2097-0382 ISSN (Online) 2097-4000

Narrow beam and low-sidelobe electro-optic beam steering on thin-film lithium niobate optical phased array

Yang Li, Shiyao Deng, Xiao Ma, Ziliang Fang, Shufeng Li, Weikang Xu, Fangheng Fu, Xu Ouyang, Yuming Wei, Tiefeng Yang, Heyuan Guan* and Huihui Lu*

Citation: Li Y, Deng SY, Ma X et al. Narrow beam and low-sidelobe electro-optic beam steering on thin-film lithium niobate optical phased array. *Opto-Electron Sci* **5**, 260002 (2026).

https://doi.org/10.29026/oes.2026.260002

Received: 23 January 2026; Accepted: 9 February 2026; Published online: 12 February 2026

Related articles

High fiber-to-fiber net gain in erbium-doped thin film lithium niobate waveguide amplifier as an external gain chip

Jinli Han, Mengqi Li, Rongbo Wu et al

Opto-Electronic Science 2025, **4**(9): 250004 doi: 10.29026/oes.2025.250004

Thin-film lithium niobate-based detector: recent advances and perspectives

Xiaoli Sun, Yuechen Jia, Feng Chen

Opto-Electronic Science 2025, **4**(12): 250028 doi: 10.29026/oes.2025.250028

Strong-confinement low-index-rib-loaded waveguide structure for etchless thin-film integrated photonics

Yifan Qi, Gongcheng Yue, Ting Hao et al

Opto-Electronic Advances 2025, **8**(9): 250056 doi: 10.29026/oea.2025.250056

Ultra-high-Q photonic crystal nanobeam cavity for etchless lithium niobate on insulator (LNOI) platform

Zhi Jiang, Cizhe Fang, Xu Ran et al

Opto-Electronic Advances 2025, **8**(1): 240114 doi: 10.29026/oea.2025.240114

More related articles in Opto-Electronic Journals Group website

Opto-Electronic Science

Article

February 2026, Vol. 5, No. 2

Open Access

Narrow beam and low-sidelobe electro-optic beam steering on thin-film lithium niobate optical phased array

Yang Li[1,2], Shiyao Deng[1,2], Xiao Ma[1,2], Ziliang Fang[1,2], Shufeng Li[1,2], Weikang Xu[1,2], Fangheng Fu[1], Xu Ouyang[1], Yuming Wei[2], Tiefeng Yang[1], Heyuan Guan[2]* and Huihui Lu[1,2]*

Abstract: Optical beam steering has become indispensable in free-space optical communications, light detection and ranging (LiDAR), mapping, and projection. Optical phased array (OPA) leads this field as versatile and miniaturized platform to this end, yet conventional versions still suffer from a narrow steering field of view, insufficient sidelobe suppression, and limited angular resolution in electro-optic (EO) beam steering. Thin-film lithium niobate (LN), with its strong EO effect, offers a powerful integrated-photonics platform to overcome these limitations. Here we present a two-dimensional (2D) EO-steered OPA based on a non-uniformly spaced X-cut thin-film LN ridge-waveguide array. A superlattice ridge design suppresses optical crosstalk to −20 dB, enabling low-sidelobe far-field radiation. Using particle swarm optimization method, we transform a uniformly spaced waveguide array into an optimized non-uniform design, largely improving angular resolution while maintaining sidelobe suppression. When combined with a single-radiating trapezoidal end-fire emitter incorporating an etched grating, the device produces a main-lobe beam with fine width of 0.99°×0.63° from an aperture of only 140 μm×250 μm, achieving a wide 2D steering range of 47°×9.36° with a 20 dB sidelobe-suppression ratio. These results highlight thin-film LN OPA as a compelling route toward ultra-compact, high-performance high-speed EO beam-steering modules and optical free-space modulators.

Keywords: non-uniform lithium niobate waveguide arrays; superlattice waveguide; optical beam steering; narrow beam; low sidelobe

DOI: 10.29026/oes.2026.260002 | CSTR: 32246.14.oes.2026.260002

Citation: Li Y, Deng SY, Ma X et al. Narrow beam and low-sidelobe electro-optic beam steering on thin-film lithium niobate optical phased array. *Opto-Electron Sci* **5**, 260002 (2026).

1 Introduction

Optical modulation has become a cornerstone of modern photonics, underpinning space communications, photonic computing, and advanced imaging while continually opening new avenues for research and application. In today's era of ultra-high-speed, ultra-high-capacity data exchange, the demands on information-processing hardware have never been greater. Optical beam modulation—dynamic steering of light to a prescribed direction—now plays an indispensable role in many photonic systems[1,2]. By changing a beam's propagation vector in free space, beam-scanning techniques provide the precise pointing needed for free-space optical links[3], optical switching[4], light detection and ranging (LiDAR)[5–8], and laser display technologies[9]. Robust control of beam direction thus forms the linchpin for target detection, tracking, recognition, and high-resolution imaging. High-performance photonic chips and devices constitute the core of optical beam-steering technology, enabling the transmission, reception, and processing of photon signals. LiDAR systems today employ two main classes of steering mechanisms: mechanical solutions—such as rotating mirrors and micro-electro-mechanical system (MEMS)[10]—and non-mechanical alternatives. Overall, optical beam steering can be categorized into four approaches: mechanic, acousto-optic, thermo-optic, and electro-optic (EO). Mechanical scanners are inherently bulky, require complex drive electronics, and suffer from low reliability and high fabrication

Received: 23 January 2026

Accepted: 9 February 2026

Published online: 12 February 2026

[1]Guangdong Provincial Key Laboratory of Optical Fiber Sensing and Communications, Jinan University, Guangzhou 510632, China; [2]International Cooperation Joint Laboratory for Optoelectronic Hybrid Integrated Circuits, Jinan University, Guangzhou 510632, China.

*Correspondence: HY Guan, E-mail: ttguanheyuan@jnu.edu.cn; HH Lu, E-mail: thuihuilu@jnu.edu.cn

costs. Moreover, their inertia limits steering speed, making them increasingly unable to meet the rapid-response demands of modern information systems[11]. Optical phased array (OPA) has emerged as a next-generation beam-steering solution[12], offering compact footprints, high steering speeds, and precise control after decades of refinement. By independently modulating the phase of each sub-aperture, an OPA shapes the interference pattern of the composite beam, enabling agile, programmable beam direction. This capability underpins a wide—and rapidly expanding—range of applications in optical data storage and processing, free-space optical communications, and LiDAR, making OPA a major focus of international research.

Integrated photonic platforms for OPAs span silicon[13,14], thin-film lithium niobate ($LiNbO_3$, LN)[15–17], III–V compound semiconductors[18], phase-change polymers, lithium tantalate[19], etc. Yet conventional OPA designs still face limited steering range and insufficient sidelobe suppression, motivating structural innovations and new material choices. Silicon-based OPAs leverage CMOS fabrication and low cost, but their thermo-optic tuning yields high power consumption and low speed. Furthermore, EO polymers are one of important candidate materials for OPA. For example, an EO-polymer OPA with organic silica for cladding and the characteristics of the eight-channel-waveguide OPA were experimentally investigated, which enabled a steering field of view (FOV) of 19.1° and a beam width of 3.9° at a high scanning frequency of 2 MHz[20]. Nevertheless, unlike LN, EO polymers do not rely on their own ferroelectric properties to achieve EO modulation. Their material properties are not stable enough and are easily affected by the experimental environment, which leads to a decrease in phase modulation accuracy for optoelectronic applications. In addition, the propagation loss of EO polymer waveguides is significantly higher than that of LN waveguides. Thin-film LN (TFLN) waveguides, by contrast, offer ultralow propagation loss—down to 0.027 dB/cm—and a large EO coefficient ($\gamma_{33} = 30.9$ pm/V)[21], enabling efficient, fast phase modulation without thermal overhead. As semiconductor processing for TFLN matures[22], LN ridge-waveguide OPAs based on EO beam steering are poised to deliver wider steering angles, lower sidelobes, faster response speed, and lower power operation, positioning them as a promising platform for next-generation beam steering across communications, computing, and sensing. More recently, there have been successful LN OPAs for two-dimensional (2D) beam steering reported[23–25]. On the other hand, the on-chip LN OPAs based on phase modulators for high-speed 2D scanning has been demonstrated[26,27]. However, it should be noted that previously reported TFLN OPAs for EO beam steering do not simultaneously achieve efficient sidelobe suppression and narrow beam width, which limit its further application.

Herein, we present a 16-channel thin-film lithium niobate optical phased-array (TFLN-OPA) chip that combines a superlattice waveguide array with non-uniform widths and a trapezoidal grating emitter. A particle-swarm-optimization (PSO) algorithm refines the geometric parameters, boosting overall performance. After the fabricated chip is experimentally characterized, it delivers 20 dB sidelobe suppression and an angular resolution of 0.99°×0.63°. EO phase tuning together with wavelength sweeping further enables a wide 2D steering FOV of 47°×9.36°, underscoring the chip's potential for high-precision, high-efficiency beam control. Overall, this work demonstrates the capability of high resolution and wide-angle beam steering using such an OPA benefiting from the combination of different structures.

2 Device structure and characteristics

TFLN is an excellent platform for high-performance EO modulation thanks to its exceptional material properties. LN exhibits pronounced birefringence at an incident wavelength of 1550 nm, with an extraordinary refractive index (n_e) of 2.14. Figure 1(a) depicts the proposed TFLN OPA: a low-loss edge coupler feeds a cascade of 1×2 power splitters that evenly distribute the input light into 16 channels. To maximize the EO coefficient of LN crystal, the device is fabricated on X-cut TFLN, with the optical axis (Z-axis) lying in the chip plane and perpendicular to the waveguide propagation direction (Y-axis). Combined with a near-half-etched TFLN ridge waveguide (250 nm thick) and a silicon dioxide (SiO_2) cladding layer, they work together to minimize optical propagation loss. Mode-field simulations of a single ridge waveguide in the OPA yield optimal dimensions of 980 nm waveguide width (w_{LN_bottom}) and 250 nm etch depth (h_{LN_etch}), giving an estimated loss of just 0.015 dB/cm.

Then, etched TFLN inverted double-layer tapered waveguide and silicon oxynitride (SiON) are adopted to construct the spot size converter (SSC) as the edge coupler for efficient coupling (details can be found in Supplementary information Section 1). In addition, the waveguide bending radius is set to 100 μm to reduce bending losses of OPA device. A binary tree of 1×2 multimode interferences (MMIs) connected by bend waveguides, which have a 1130 μm bending radius for achieving low excess loss and minimal beam degradation in the curved waveguides, is used for power splitting. As Fig. 1(b) shows, the device operates with transverse electrically (TE)-polarized light, which offers stronger mode confinement than transverse magnetic (TM) polarization in this single-mode LN waveguide.

Furthermore, each of the 16 channels incorporates a 5 mm-long EO phase shifter. Electrodes separated by a 4 μm gap (see Fig. 1(c)) maximize microwave-optical overlap; because LN has a high microwave permittivity, the electric field concentrates mainly in the surrounding SiO_2 rather than in the ridge core. Optimizing the transmission-line structure gives electrode dimensions of 40 μm (signal), 100 μm (ground), and 1000 nm thickness, balancing low drive voltage with minimal loss.

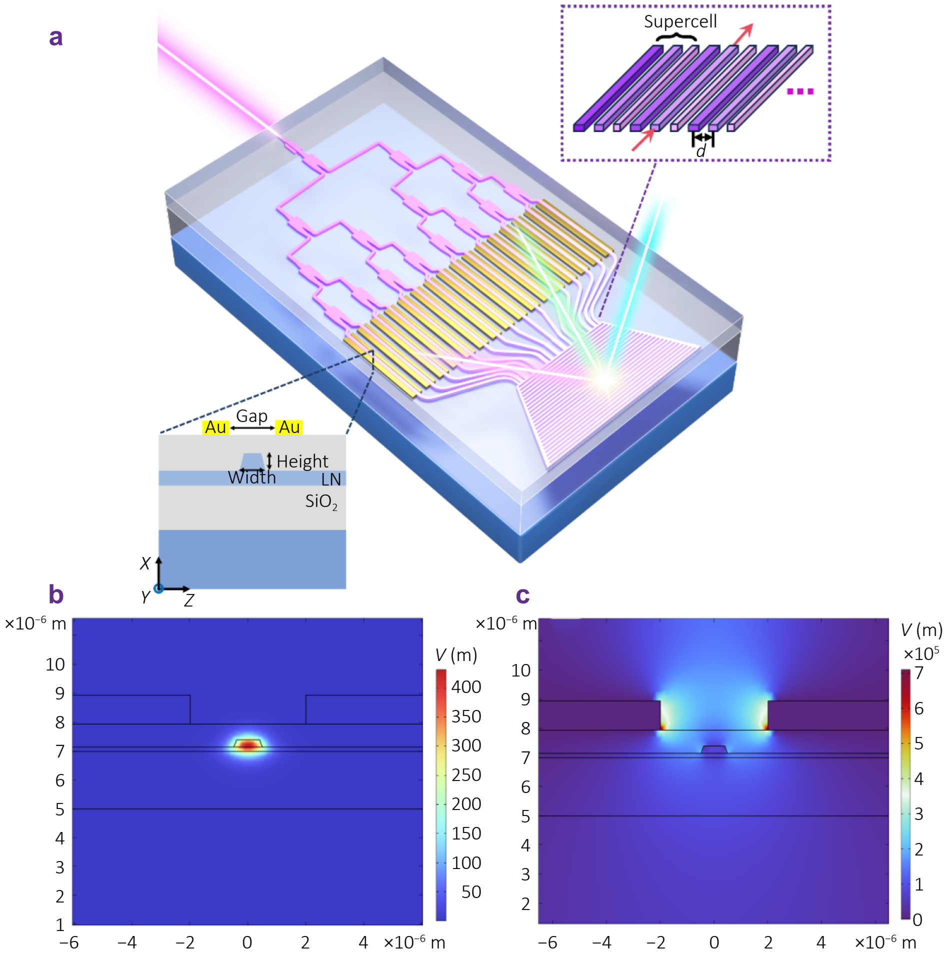

Fig. 1 | (a) Schematic diagram of the 1 × 16 TFLN-based OPA with non-uniformly spaced waveguides. The optical axis is aligned with the *Z*-axis, while the incident beam propagates along the *Y*-axis. The top-right inset illustrates the superlattice layout in the beam-combining region, and the bottom-left inset shows the cross-section of the TFLN ridge waveguide. (b) Simulated TE-mode profile at a 1550 nm wavelength in the TFLN ridge waveguide. (c) Simulated electric-field distribution when a 1 V bias is applied to the LN waveguide electrodes.

To more effectively adjust the propagation mode of beam, the waveguides in the beam-combining region are patterned into a periodic superlattice whose widths are precisely engineered. Meanwhile, this deliberate modulation of structural parameters provides additional control over light propagation while the alternating-width pattern markedly suppresses crosstalk between adjacent channels[28]. As illustrated in the upper-right inset of Fig. 1(a), the beam-combining section employs a periodic superlattice in which every supercell (SC) comprises three waveguides of distinct widths $w_1 > w_2 > w_3$. All channels share a uniform center-to-center pitch d, and light propagates in the direction marked by the red arrow. Fabrication limits dictate the upper and lower bounds of the waveguide width, within which the three values are judiciously spaced. Adopting a monotonically descending width sequence inside each supercell minimizes phase mismatch among neighboring guides and thereby suppresses optical crosstalk, which refers to the normalized power coupled from one waveguide into an adjacent one[29,30].

The proposed waveguide superlattice can utilize the difference in the width of adjacent waveguides to minimize the coupling between array elements, thereby effectively reducing the optical crosstalk in the combining region of the OPA. The waveguide width used in the OPA based on uniform spacing distribution is 980 nm. Taking the average waveguide width available in the preparation process as the reference, the superlattices with different waveguide widths of n are obtained by alternating arrangement. The far-field radiation intensity spectra shown in Fig. 2 is obtained for comparative analysis.

For comparison, Fig. 2 presents the resulting far-field radiation spectra obtained from 1 × 16 TFLN OPA based on different waveguide width periods, namely: uniform waveguide width array, with waveguide widths of 980 nm for all; superlattice waveguide SC2, whose waveguide widths alternate between 980 nm and 860 nm; superlattice waveguide SC3, whose waveguide widths follow a three-element cycle of 1040 nm, 980 nm, and 920 nm. Insets show the corresponding waveguide width-period schematics. To the best of our knowledge, the highest-intensity beam is designated as the main lobe in each far-field pattern, while subsidiary peaks are side lobes. The peak side lobe level (PSLL) quantifies the strongest side lobe relative to the main lobe and is expressed in decibels (dB). Based on this definition, the PSLL can be calculated as[31]:

$$PSLL = 10 \cdot \log_{10}\left(\frac{I_{\text{Maxsidelobe}}}{I_{\text{Mainlobe}}}\right)(\text{dB}) . \quad (1)$$

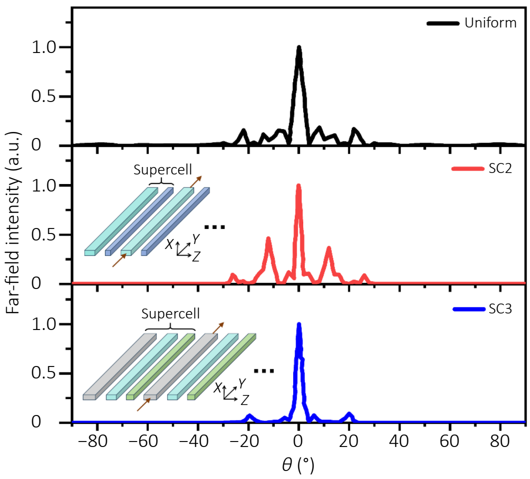

Fig. 2 | Numerical simulations of the 1×16 TFLN-based OPA reveal how the waveguide-array geometry shapes the far-field beam intensity profile. The output beams of three designs are compared: the uniform array, with the waveguide width of all being 980 nm; superlattice waveguide SC2, whose waveguide width periods are 980 nm and 860 nm, respectively; superlattice waveguide SC3, whose waveguide width periods are 1040 nm, 980 nm, and 920 nm, respectively. Insets in each spectrum sketch the corresponding width patterns, with color coding denoting the different waveguide widths.

Analysis shows that the SC3 superlattice design drives the PSLL down to roughly −10 dB while keeping overall output-power uniformity of the array within about −20 dB.

To concentrate energy in the main lobe and suppress superlattice side lobes, we employ an appropriate PSO algorithm[32,33] to fine-tune the spacing between waveguide elements (see in the Supplementary information Section 2). The fitness function weighs two metrics from the array's simulated far-field pattern: the PSLL and the main-lobe width, quantified by the full width at half maximum (FWHM). By iteratively updating the inter-element spacing, the PSO converges on a configuration that simultaneously minimizes PSLL and shrinks the FWHM. According to the FWHM expression for the far-field pattern[12]:

$$\theta_{\text{FWHM}} = \frac{0.886\lambda}{Nd\cos\theta_{\text{BeamSteering}}} , \quad (2)$$

where N, d and $\theta_{\text{BeamSteering}}$ represent the number of array elements, element spacing and steering angle, respectively. Thus, the effective way to improve the trade-off between beam steering range and beam resolution is to increase the number of elements. However, the increase in the number of arrays will bring additional optical loss and fabrication difficulty. Therefore, the 1×16 OPA device obtained by PSO optimization can maintain a smaller number of arrays while considering high-resolution beam steering.

It is noteworthy to discuss the emission region of the OPA. In our case, we choose the end-fire trapezoidal plate length $L_{\text{Trapezoid}}$ as 350 μm according to the process requirements. To narrow the main lobe width of the far-field output beam, further simulation and binary optimization are carried out on the top and bottom widths of the emitting trapezoidal plate, as shown in Fig. 3(a) and 3(b). In addition, the flat grating is designed to be trapezoidal in shape, and a suitable tilt angle needs to be selected to make it larger than the in-plane divergence angle of the flat mode, so that more than 90% of the beam power can be transmitted forward freely without being affected by the reflection of the side walls[26]. The optimal trapezoidal plate width selected needs to comprehensively consider its corresponding far-field sidelobe suppression ratio (as shown in Fig. 3(a)) and the far-field beam main lobe width (as shown in Fig. 3(b)). After comprehensive consideration, the optimal values are $W_{\text{Trapezoid\_short}}$=140 μm and $W_{\text{Trapezoid\_long}}$=250 μm.

Earlier research work has shown that etching a periodic groove structure on the emitting array of a LN waveguide array to form a grating array antenna is an effective solution to improve the quality of its output beam, which helps to achieve the shaping and steering of narrower steering beam. Therefore, the etched grating on a trapezoidal plate as the end-fire of OPA is proposed, rather than using multiple emitting arrays such as a grating antenna array. When the optical waveguide mode propagates to the trapezoidal grating, the waveguide mode will be transformed into a plate divergent mode due to the in-plane interference steering combined with the out-of-plane radiation of the etched grating. Moreover, in this work, the optimal value of the etched grating thickness of 140 nm is obtained by almost half-etching the thickness of the LN ridge waveguide. The width of the etched grating used here is of the gradient type, and it will be reasonably designed according to the structural parameters of the end-fire trapezoidal plate. In order to obtain the optimal output beam steering performance of the trapezoidal plate etched grating, we conduct a binary optimization analysis on the period and duty cycle of the etched grating based on the performance indicators of the steering beam, such as the sidelobe suppression and its far-field main lobe beam width. The optimization range is the etched grating period of 800–1600 nm, and the grating duty cycle of 0.4–0.6.

Figure 3(c) and 3(d) respectively show the binary optimization results of PSLL and FWHM obtained by etching

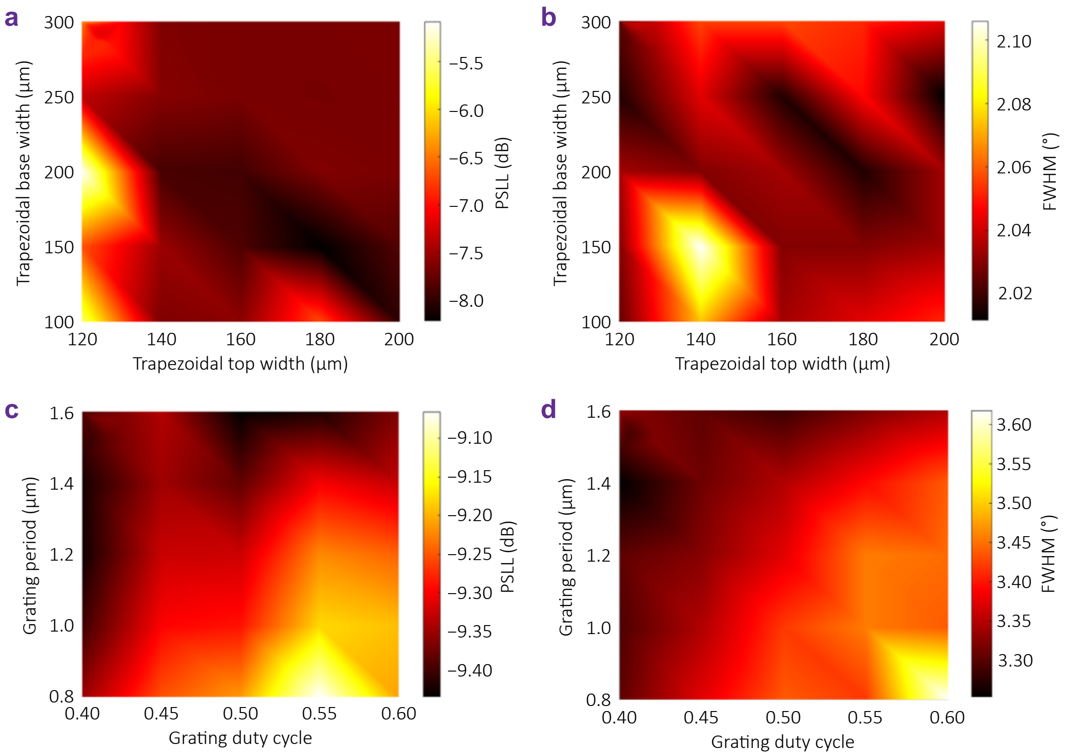

Fig. 3 | Numerical analysis of the trapezoidal transmitting grating structure in OPA. (a) When the length of the trapezoidal plate is 350 μm, the result of PSLL obtained by optimizing the upper and lower widths of the trapezoidal plate. (b) Optimization results of FWHM obtained for the upper and lower widths of the trapezoidal plate. (c) Simulation optimization results of PSLL obtained by etching grating period and its duty cycle. (d) Simulation optimization results of FWHM obtained by etching grating period and its duty cycle.

the grating period and its duty cycle. It can be analyzed that the structural etching depth of the optimized width-gradient SiO_2 grating in this work is 140 nm, and the etching period length of the grating is 500 nm, corresponding to a duty cycle of 0.5.

Based on the proposed 16-channel TFLN OPA by EO steering, high-precision processing technology is used to complete chip preparation and experimental characterization for subsequent experimental research. The fabrication of the OPA chip by hard mask etching (more details can be found in Supplementary information Section 3) is mainly accomplished through technologies such as electron beam lithography (EBL), inductive coupled plasma (ICP) etching, and plasma-enhanced chemical vapor deposition (PECVD). Based on this scheme, the OPA chip is fabricated on a commercial X-cut TFLN wafer, which consists of a 400 nm-thick LN layer, a 2 μm SiO_2 layer, and a 525 μm silicon substrate layer. This multilayer structure design ensures good optical confinement effect and mechanical stability of device. The top width of the LN ridge waveguide is 980 nm, which is optimized for better single-mode transmission. The etching depth of the LN waveguide layer is 250 nm, ensuring good optical mode confinement. On the other hand, the SiO_2 coating is deposited using PECVD technology to improve the mode field distribution and provide protection. The fabricated TFLN-OPA chip is visually presented through optical microscopy characterization, as shown in Fig. 4(a), which is the microscopic image of the well-prepared OPA chip for realizing 2D beam steering.

Figure 4(b–e) are electron microscope images showing the basic components of the magnified OPA chip, including the zoomed-in SSC, the corresponding MMIs based on LN ridge waveguide, the optical phase shifters of the chip and the electrode structure distributed at both ends, and the beam combining region and the transmitting end of the phased array. It includes the microscopic diagram of the superlattice waveguide array and trapezoidal emission grating. The fabricated 16-channel OPA with an appropriate sparse non-uniform antenna spacing can be used to suppress the grating lobes and higher resolution beam steering.

3 Experimental results and discussions

In general, higher resolution can be obtained by compressing the optical beam divergence, which requires a larger aperture. According to the far-field theory ($n_{\text{eff}}A^2/(D\lambda) < 1$)[34,35], where A is the aperture size of the OPA, λ is the operating wavelength, D is the distance of the observation point from the array, and n_{eff} is the effective refractive index of propagation inside the LN ridged waveguide. The proposed OPA based on chip-scale TFLN

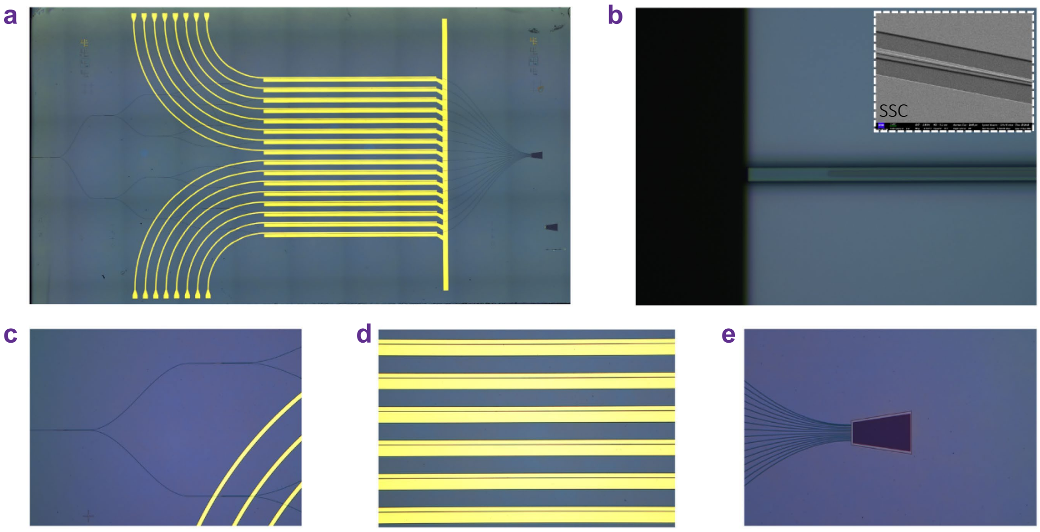

Fig. 4 | Optical micrographs of the fabricated OPA chip and its basic components. (a) Optical microscopy of the non-uniform TFLN-OPA chip. (b) Designed spot size converter (SSC) at the incident end of the chip, with its scanning electron microscopy (SEM) image in the inset. (c) Microscope of MMIs. (d) Micrograph of a portion of the optical phase shifter and the electrodes at its two ends. (e) Micrograph of the beam combining region and the transmitting end of the phased array, including superlattice waveguide array and trapezoidal emission grating.

platform can achieve 2D beam steering. To show this capability, the small optical aperture of 140 μm × 250 μm is designed to obtain high-resolution beam steering. The experimental setup for OPA is schematically shown in Fig. 5(a). To characterize the optical performance of the fabricated OPA chip, we have used a continuous-wave tunable laser source (AQ2200-136) to generate light ranging from 1440 nm to 1640 nm. Moreover, it is necessary to connect special optical fiber (Ultra-High Numerical Aperture 7, namely UHNA-7) to achieve efficient edge coupling between the optical fiber and the device under test (DUT). As noted, the incident laser is set to the fundamental transverse electric (TE_0) mode, which can be controlled by the polarization controller (PC). The far-field pattern distribution is captured by a charge coupled device (CCD). A CCD camera captures top-down images of the scattered light at the designed TFLN OPA. The emission from the OPA chip is collected by an objective lens with a numerical aperture (NA) of 0.4 and expanded through a 4-*f* system to fit the CCD camera.

As shown in Fig. 5(b), the 16-channel TFLN OPA is fabricated on a 2.1 cm × 2 cm X-cut lithium niobate on insulator (LNOI) chip, which is wire-bonded on a printed circuit board (PCB) and controlled by the circuit control system that has been built. In practice, due to the inevitable technological errors in the chip processing, it is difficult to ensure that the initial phase of each radiation beam remains the same as theoretical design value. Therefore, it is necessary to

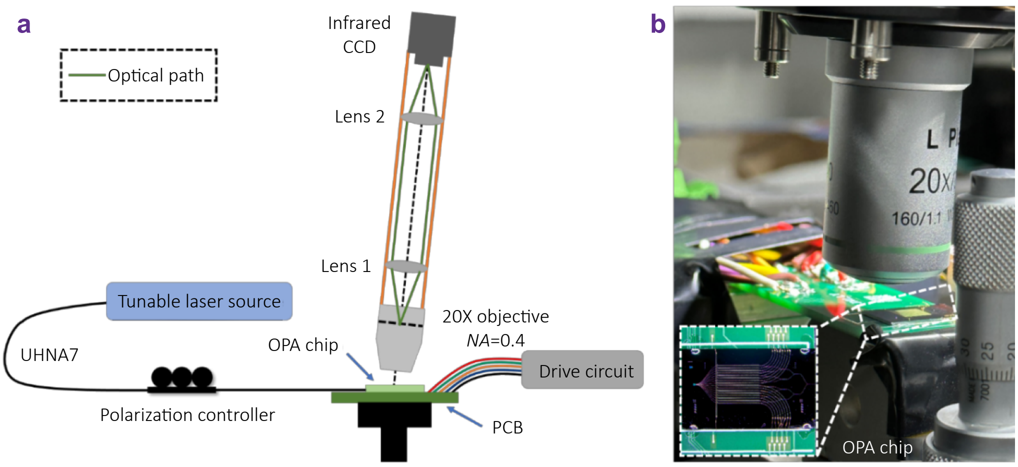

Fig. 5 | Experimental setup of the device under test (DUT). (a) Schematic diagram of the experimental setup for near-field and far-field testing of TFLN-OPA chip. (b) Photograph of the part of the experimental setup. The OPA chip is mounted on a printed circuit board (PCB).

adopt the phase optimization calibration method to achieve precise pointing of the radiation beam. As presented in Fig. 6(a), when no voltage is applied to the OPA, multiple scattered light spots of varying brightness can be clearly seen in the initial far-field interference pattern obtained.

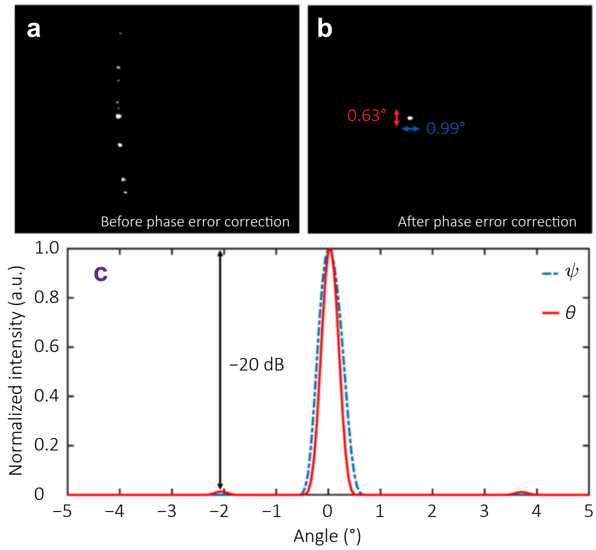

Fig. 6 | Far-field radiation spot before and after initial phase error calibration at optical wavelength of 1550 nm. (a) Far-field pattern before phase error calibration. (b) Far-field beam pattern after phase error calibration, with a well-focused main beam, showing the main-lobe width of 0.99°×0.63°. (c) Normalized far-field radiation intensity spectrum, presenting the optimized sidelobe suppression up to −20 dB.

At this time, the main lobe and side lobe of the far-field beam cannot be distinguished. This is due to the initial phase difference between adjacent waveguides of the phase shifter. The EO phase is randomly distributed, resulting in the dispersion of the beam energy. To address this issue, it is necessary to perform initial phase calibration on the chip. Then, by optimizing and adjusting each voltage applied to the phase shifters of OPA, the emitted light spot is optimized to the brightest single-mode far-field spot as shown in Fig. 6(b). Thus, the calibration of the initial phase error of the chip is completed. At an operating wavelength of 1550 nm, the far-field beam has a FWHM spot size of 0.99°×0.63°.

Moreover, it can be known from the normalized beam spectra obtained in the longitudinal and lateral directions of the far-field radiation as plotted in Fig. 6(c), which can be seen that the calculated PSLL can be as low as −20 dB. Theoretically, a scanning beam with both PSLL and high resolution can be achieved through PSO. Furthermore, experimentally, optimizing the random distribution of voltage not only eliminates additional phase differences but also further improves the overall sidelobe suppression performance to −20 dB, which effectively verifies the necessity of completing the phase error calibration by the optimized feedback of EO controlled phase of each channel waveguide during the experimental test. Further as mentioned above, the experimental research on the beam steering of the chip is continued.

In this work, the incident laser is edge-coupled into the waveguide and modulated by 16-channel EO phase shifters integrated on the TFLN-OPA chip. Considering the excellent EO properties of LN, the proposed OPA can theoretically achieve a half-wave voltage-length product of approximately 4.1 V·cm. Figure 7(a) illustrates longitudinal beam steering in the far field is achieved by applying optimized voltages to the 5-mm-long modulation region of OPA chip. Then the steering angle θ of the EO modulated light beam is theoretically given as[36]:

$$\sin\theta = \frac{\lambda\Delta\varphi}{2\pi d}\ , \tag{3}$$

here, $\Delta\varphi$ refers to the phase difference between the waveguide arrays. d represents the array spacing of the OPA, and the operating wavelength is denoted by λ. As is evident, the side lobes of the measured far-field pattern are −13 dB, which can be tuned to approximately 47°, corresponding to a π-phase shift of the aperiodic antenna pattern, as presented in Fig. 7(b).

Additionally, the RC-limited modulation bandwidth can be calculated up to 0.96 GHz with an estimated capacitance of 2.5 pF. The electrical energy for inducing a phase shift of π can indicate the low power consumption of 42.2 pJ/π per EO modulator. The grating emitter of OPA emits light. Based on the grating diffraction theory, the OPA chip can perform wavelength-tuned beam steering by changing the incident light wavelength (near-field experiment can be seen in Supplementary information Section 4). The steering of the beam in the lateral dimension direction achieved by tuning the wavelength, with the output coupling angle ψ controlled by the grating equation as follows[37]:

$$\sin\psi = \frac{\Lambda n_{\text{eff}} - \lambda}{n_0 \Lambda}\ , \tag{4}$$

where Λ is the grating period, λ is the laser wavelength, n_{eff} is the effective index of the waveguide mode, and n_0 is the index of the background. In the experiment, wavelength-dependent measurements are performed to help validate second-dimensional beam steering, as demonstrated in Fig. 7(c). By sweeping the input wavelength range from 1510 nm to 1610 nm, the steering range of the emitted light in the ψ-direction is 9.36°, with PSLL of −12 dB, as shown in Fig. 7(d).

Based on the above analysis, the proposed TFLN-OPA chip can achieve a wide beam steering range of 47°×9.36° with low sidelobe in the phased-array steering axis and the wavelength-tuning steering axis. In addition, multiple output far-field radiation modes can be obtained through wavelength tuning and phase EO modulation to superimpose and synthesize arbitrary images, such as the 2D beam

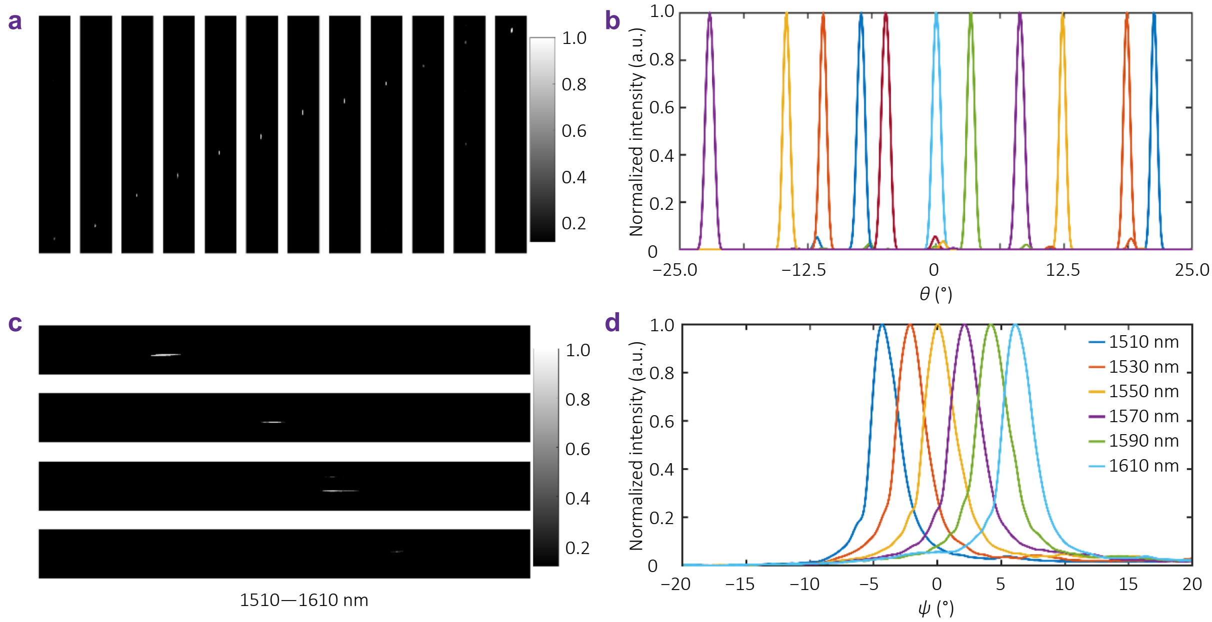

Fig. 7 | 2D beam scanning of TFLN-OPA chip. (a) Far-field radiation pattern at different steering angles obtained after applying an external voltage for phase modulation with a fixed incident wavelength of 1550 nm. (b) Measured relationship between the output power distribution and the EO modulation angle. As the applied voltage changes, the steering FOV is 47°, and the corresponding PSLL is −13 dB. (c) Far-field radiation distribution obtained by changing the wavelength of the incident laser from 1510 nm to 1610 nm. (d) Measured relationship between the output optical power distribution and the wavelength tuning angle. As the wavelength changes, the steering FOV is 9.36° and its PSLL is −12 dB.

trajectory EO modulated writing of the capital letter "JNU" shown in Fig. 8.

As a result, the OPA chip can scan the high-resolution optical beam with side lobes suppression. Notably, the steering range will be limited by the NA of objective lens, which has an acceptance angle of 48° yields. To maximize the observable FOV, devices such as rotating disks can be added to expand the far-field radiation steering range of the OPA device. Table 1 shows recent work on different kinds of OPAs compared with our work. By comparing and analyzing the optical beam steering performance of other OPAs, the TFLN-OPA chip in this work has a relatively low PSLL, and can achieve a larger steering FOV while maintaining a higher resolution. Its modulation speed is relatively fast. The results show that the proposed TFLN OPA obtains a low PSLL and finer beam with relative wide-FOV optical beam steering for only 16 channel waveguides.

4 Conclusions

In conclusion, an effective solution for suppressing sidelobes in the TFLN-based OPA with high-resolution 2D beam steering has been proposed and experimentally demonstrated. This study optimizes the waveguide array geometry and validates beam-steering performance through simulation and experiment. First, superlattice width is introduced to the waveguide array, significantly lowering optical crosstalk and reducing sidelobe levels. Next, a PSO routine

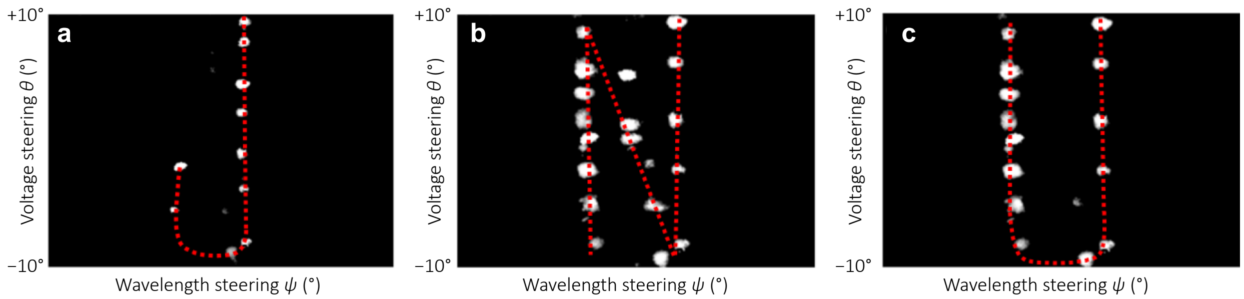

Fig. 8 | By simultaneously controlling the wavelength tuning and the phase modulation of the OPA chip, the far-field radiation pattern obtained within the steering FOV is superimposed to synthesize the 2D images of the three letters "JNU", which are (a) "J"; (b) "N"; (c) "U". Among them, the obtained far-field beam composite images are all depicted and fitted with red dotted lines for viewing.

Table 1 | Performance summary and comparison of the reported OPAs.

Process technology (Channels)	Modulation mechanism	PSLL (dB)	Steering FOV	FWHM	Bandwidth	Power consumption
Si OPA[38] (1×64)	Charge-injection	−8.8	8.9°×2.2°	0.92°×0.32°	324 MHz	17 mW/π
Si OPA[39] (1×64)	Carrier depletion	−10	36°×3.4°	0.85°×0.25°	700 MHz	0.45 nW/π
Polymer waveguides[20] (1×8)	EO effect	*N/A*	19.1°	3.9°	2 MHz	47.5 μW/π
InP OPA[40] (1×8)	EO effect	−11.7±1.8	18°	2.48°±0.3°	*N/A*	*N/A*
LN OPA[23] (1×16)	EO effect	−10	24°×8°	2°×0.6°	4.2 GHz	13.5 pJ/π
TFLN OPA[26] (1×16)	EO effect	−5.3	50°×8.6°	0.73°×2.8°	2.5 GHz	330 pJ/π
TFLN OPA[27] (1×32/48)	EO effect	−7.4	62.2°×8.8° 40°×8.8°	2.4°×1.2° 0.33°×1.8°	69 MHz	1.11 nJ/π
TFLN-SiN OPA[24] (1×16)	EO effect	*N/A*	22°×5°	1.2°×0.2°	1.2 GHz	3.2 pJ/π
End-fire OPA on TFLN[41] (1×16)	Waveguide dispersion	*N/A*	15°	1.6°	*N/A*	*N/A*
Visible-light OPA on TFLN[42] (1×32)	EO effect	−7.5	40°	1.14°×0.41°	5.4 GHz	*N/A*
TFLN OPA (1×16) (This work)	**EO effect**	**−20**	**47°×9.36°**	**0.99°×0.63°**	**0.96 GHz**	**42.2 pJ/π**

converts the uniformly spaced array into a non-uniform configuration, balancing sidelobe suppression with enhanced steering resolution. In addition, the trapezoidal grating emitter of the chip is systematically simulated and analyzed to achieve more efficient far-field radiation. The fabricated 1×16 TFLN OPA, featuring optimized non-uniform emitter spacing and a compact 140 μm×250 μm aperture, delivers a main-beam resolution of approximately 0.99°×0.63°. EO phase tuning and wavelength sweeping enable a wide steering FOV of 47°×9.36°, while sidelobe levels are held 20 dB below the main lobe. These results confirm the excellent EO beam steering performance of the OPA, highlighting TFLN as a promising platform for ultra-compact, high-performance optical beam modulation devices.

References

1. Warger II WC, DiMarzio CA. Dual-wedge scanning confocal reflectance microscope. *Opt Lett* **32**, 2140–2142 (2007).
2. Heck MJR. Highly integrated optical phased arrays: photonic integrated circuits for optical beam shaping and beam steering. *Nanophotonics* **6**, 93–107 (2017).
3. Reza SA, Riza NA. A liquid lens-based broadband variable fiber optical attenuator. *Opt Commun* **282**, 1298–1303 (2009).
4. Shang JM, Chen HJ, Sui Z et al. Electro-optic high-speed optical beam shifting based on a lithium niobate tapered waveguide. *Opt Express* **30**, 14530–14537 (2022).
5. Xie YW, Hong SH, Yan H et al. Low-loss chip-scale programmable silicon photonic processor. *Opto-Electron Adv* **6**, 220030 (2023).
6. Beiser L. Fundamental architecture of optical scanning systems. *Appl Opt* **34**, 7307–7317 (1995).
7. Mirmozafari M, Zhang ZT, Gao M et al. Mechanically reconfigurable, beam-scanning reflectarray and transmitarray antennas: a review. *Appl Sci* **11**, 6890 (2021).
8. Zhu S, Zhang YW, Feng JX et al. Integrated lithium niobate photonic millimetre-wave radar. *Nat Photonics* **19**, 204–211 (2025).
9. Chen HW, Weng YS, Xu DM et al. Beam steering for virtual/augmented reality displays with a cycloidal diffractive waveplate. *Opt Express* **24**, 7287–7298 (2016).
10. Meng C, Thrane PCV, Ding F et al. Dynamic piezoelectric MEMS-based optical metasurfaces. *Sci Adv* **7**, eabg5639 (2021).
11. Wang YM, Zhou GY, Zhang XS et al. 2D broadband beamsteering with large-scale MEMS optical phased array. *Optica* **6**, 557–562 (2019).
12. McManamon PF, Dorschner TA, Corkum DL et al. Optical phased array technology. *Proc IEEE* **84**, 268–298 (1996).
13. Sun CM, Yang LS, Li BH et al. Parallel emitted silicon nitride nanophotonic phased arrays for two-dimensional beam steering. *Opt Lett* **46**, 5699–5702 (2021).
14. Qiu HQ, Liu Y, Meng XS et al. Ultra-sparse aperiodic silicon optical phased array using high-performance thermo-optic phase shifter. *Laser Photonics Rev* **18**, 2301177 (2024).
15. Pan BC, Liu HX, Huang YS et al. Perspective on lithium-niobate-on-insulator photonics utilizing the electro-optic and acousto-optic effects. *ACS Photonics* **10**, 2078–2090 (2023).
16. Li JW, Zheng HB, Han YY et al. Design and analysis of single-electrode integrated lithium niobate optical phased array for two-dimensional beam steering. *Opt Lasers Eng* **184**, 108617 (2025).
17. Han JL, Li MQ, Wu RB et al. High fiber-to-fiber net gain in erbium-doped thin film lithium niobate waveguide amplifier as an external

gain chip. *Opto-Electron Sci* **4**, 250004 (2025).
18. Guo WH, Binetti PRA, Althouse C et al. Two-dimensional optical beam steering with InP-based photonic integrated circuits. *IEEE J Sel Top Quantum Electron* **19**, 6100212 (2013).
19. Yan XS, Liu YA, Ge LC et al. High optical damage threshold on-chip lithium tantalate microdisk resonator. *Opt Lett* **45**, 4100–4103 (2020).
20. Hirano Y, Miyamoto Y, Miura M et al. High-speed optical-beam scanning by an optical phased array using electro-optic polymer waveguides. *IEEE Photonics J* **12**, 6600807 (2020).
21. Weis RS, Gaylord TK. Lithium niobate: summary of physical properties and crystal structure. *Appl Phys A* **37**, 191–203 (1985).
22. Sun XL, Jia YC, Chen F. Thin-film lithium niobate-based detector: recent advances and perspectives. *Opto-Electron Sci* **4**, 250028 (2025).
23. Yue GC, Li Y. Integrated lithium niobate optical phased array for two-dimensional beam steering. *Opt Lett* **48**, 3633–3636 (2023).
24. Lee WB, Kwon YJ, Kim DH et al. Hybrid integrated thin-film lithium niobate–silicon nitride electro-optical phased array incorporating silicon nitride grating antenna for two-dimensional beam steering. *Opt Express* **32**, 9171–9183 (2024).
25. Ma XY, Yuan MR, Li JC et al. Multi-target and ultra-high-speed optical wireless communication using a thin-film lithium niobate optical phased array. *Nat Commun* **17**, 969 (2026).
26. Li WL, Zhao X, He JH et al. High-speed 2D beam steering based on a thin-film lithium niobate optical phased array with a large field of view. *Photonics Res* **11**, 1912–1918 (2023).
27. Wang ZZ, Li XY, Ji JT et al. Fast-speed and low-power-consumption optical phased array based on lithium niobate waveguides. *Nanophotonics* **13**, 2429–2436 (2024).
28. Leng LM, Shao Y, Zhao PY et al. Waveguide superlattice-based optical phased array. *Phys Rev Appl* **15**, 014019 (2021).
29. Wang LP, Chen Z, Wang HF et al. Design of a low-crosstalk half-wavelength pitch nano-structured silicon waveguide array. *Opt Lett* **44**, 3266–3269 (2019).
30. Song WW, Gatdula R, Abbaslou S et al. High-density waveguide superlattices with low crosstalk. *Nat Commun* **6**, 7027 (2015).
31. Guo YJ, Guo YH, Li CS et al. Integrated optical phased arrays for beam forming and steering. *Appl Sci* **11**, 4017 (2021).
32. Robinson J, Rahmat-Samii Y. Particle swarm optimization in electromagnetics. *IEEE Trans Antennas Propag* **52**, 397–407 (2004).
33. Komljenovic T, Helkey R, Coldren L et al. Sparse aperiodic arrays for optical beam forming and LIDAR. *Opt Express* **25**, 2511–2528 (2017).
34. Hosseini A, Kwong D, Zhang Y et al. Modeling and experimental observation of an on-chip two-dimensional far-field interference pattern. *Appl Opt* **50**, 1822–1826 (2011).
35. Kwong D, Hosseini A, Zhang Y et al. 1×12 Unequally spaced waveguide array for actively tuned optical phased array on a silicon nanomembrane. *Appl Phys Lett* **99**, 051104 (2011).
36. Wang Q, Wang SX, Jia LX et al. Silicon nitride assisted 1×64 optical phased array based on a SOI platform. *Opt Express* **29**, 10509–10517 (2021).
37. Van Acoleyen K, Bogaerts W, Jágerská J et al. Off-chip beam steering with a one-dimensional optical phased array on silicon-on-insulator. *Opt Lett* **34**, 1477–1479 (2009).
38. Zhang HY, Zhang ZX, Lv JX et al. Fast beam steering enabled by a chip-scale optical phased array with 8×8 elements. *Opt Commun* **461**, 125267 (2020).
39. Zhang ZY, Yu H, Huang QK et al. High-speed and low-power silicon optical phased array based on the carrier-depletion mechanism. *IEEE Photonics Technol Lett* **34**, 271–274 (2022).
40. Gagino M, van Rijn MBJ, Bente EAJM et al. Broadband operation of an InP optical phased array. *IEEE Photonics Technol Lett* **34**, 541–544 (2022).
41. Wu JW, Liang ZK, Wang XY et al. End-fire optical phased array for passive beam steering on thin-film lithium niobate. *Opt Lett* **49**, 5087–5090 (2024).
42. Ye YQ, Lian DX, Chen ZS et al. Visible-light optical phased array on a thin-film lithium niobate platform for high-speed beam steering. *Opt Lett* **50**, 3090–3093 (2025).

Acknowledgements

We are grateful for financial supports from the National Key Research and Development Program of China (2023YFA1407200), the National Natural Science Foundation of China (62575130, 62405114, 12404577, 12504445, 21324102), the NSAF (U2330113, U2230111, U2030103), the Guangdong Basic and Applied Basic Research Foundation (2025A0505020051, 2025B1515020096, 2023A0505050159, 2023A1515110626), Industry-University-Research Cooperation Project of Zhuhai (2320004002614), and the Fundamental and Application Foundation Project of Guangzhou (2024A04J3974, 2025A04J5851).

Author contributions

Huihui Lu and Yang Li proposed the original idea, Yang Li conducted the designs, numerical simulations and experiments. Yang Li and Shiyao Deng fabricated the samples. Xiao Ma, Ziliang Fang and Shufeng Li helped during the experiments. Weikang Xu and Fangheng Fu involved in the investigations. Xu Ouyang, Yuming Wei, and Tiefeng Yang gave valuable guidance in the experiment. Yang Li prepared the manuscript. Heyuan Guan and Huihui Lu contributed to the discussion and the revision of manuscript. Heyuan Guan and Huihui Lu supervised the overall projects. All the authors analyzed and discussed the results.

Competing interests

The authors declare no competing financial interests.

Supplementary information

Supplementary information for this paper is available at
https://doi.org/10.29026/oes.2026.260002

Published by Editorial Office of *Opto-Electronic Science*, Institute of Optics and Electronics, Chinese Academy of Sciences.